Nano Research
2023, 16(8): 11389–11400

ISSN 1998-0124 CN 11-5974/O4
https://doi.org/10.1007/s12274-023-5872-y

Research Article

Encapsulated carbon nanotube array as a thermal interface material compatible with standard electronics packaging

Ruixiang Bai[1,§], Yangbing Wei[1,§], Jiyuan Xu[3], Xiaobo Li[1], Menglin Li[1], Ziwen Zou[1], Xinyan Huang[4], Chengyu Liu[5], Yiwei Sun[2] (✉), and Menglong Hao[1] (✉)

[1] *Key Laboratory of Energy Thermal conversion and control of Ministry of Education, National Engineering Research Center of Power Generation Control and Safety, School of Energy and Environment, Southeast University, Nanjing 210096, China*
[2] *School of Materials Science and Engineering, School of Energy and Environment, Southeast University, Nanjing 210096, China*
[3] *Nanjing Research Institute of Electronics Technology, Nanjing 210039, China*
[4] *Research Centre for Fire Engineering, Hong Kong Polytechnic University, Kowloon 999077, Hong Kong, China*
[5] *State Key Laboratory of Bioelectronics, School of Instrument Science and Engineering, Southeast University, Nanjing 210096, China*
[§] *Ruixiang Bai and Yangbing Wei contributed equally to this work.*

Received: 16 March 2023 / **Revised:** 10 May 2023 / **Accepted:** 24 May 2023

ABSTRACT

Vertically aligned carbon nanotubes arrays (VACNTs) are a promising candidate for the thermal interface material (TIM) of next-generation electronic devices due to their attractive thermal and mechanical properties. However, the environment required for synthesizing VACNTs is harsh and severely incompatible with standard device packaging processes. VACNTs' extremely low in-plane thermal conductivity also limits its performance for cooling hot spots. Here, using a transfer-and-encapsulate strategy, a two-step soldering method is developed to cap both ends of the VACNTs with copper microfoils, forming a standalone Cu-VACNTs-Cu sandwich TIM and avoiding the need to directly grow VACNTs on chip die. This new TIM is fully compatible with standard packaging, with excellent flexibility and high thermal conductivities in both in-plane and through-plane directions. The mechanical compliance behavior and mechanism, which are critical for TIM applications, are investigated in depth using *in situ* nanoindentation. The thermal performance is further verified in an actual light emitting diode (LED) cooling experiment, demonstrating low thermal resistance, good reliability, and achieving a 17 °C temperature reduction compared with state-of-the-art commercial TIMs. This study provides a viable solution to VACNTs' longstanding problem in device integration and free-end contact resistance, bringing it much closer to application and solving the critical thermal bottleneck in next-generation electronics.

KEYWORDS

vertically aligned carbon nanotube arrays (VACNTs), sandwich structure, thermal conductivity, thermal interface materials (TIMs)

1 Introduction

For decades, as electronic devices continue to increase their integration density and computing power, their power consumption and thus heat generation have also increased significantly [1–3]. As a result, device overheating has become a major bottleneck for future developments [4]. To maintain the device temperature within allowable range, more efficient, compact, and reliable heat removal solutions are required [5]. In particular, multiple interfaces in the thermal path from the die to the heat sink present the major thermal resistance, up to 50% of the total thermal resistance [6–9]. The high interfacial thermal resistance is due to the fact that, because of morphological roughness, only a limited portion of the apparent surface area actually makes contact when two solid surfaces are seemingly touching [10]. The consequence is that a large amount of heat flow must be squeezed to the small number of actual contact points, severely inhibiting overall heat flow. To improve this interfacial thermal transport, thermal interface materials (TIMs) need to be used between the two mating surfaces [11, 12]. However, the existing TIM materials are struggling to meet the cooling need of the rapidly advancing high-power electronics.

To achieve greater heat transfer efficacy, the ideal TIMs must have a high through-plane thermal conductivity and a low thermal contact resistance at a low loading pressure. The latter requires the TIM to have a high level of mechanical compliance to fill the microgaps between the two contact surfaces. Some metallic and inorganic nonmetallic materials have very attractive high thermal conductivities. For example, copper has a thermal conductivity of up to 380 $W \cdot m^{-1} \cdot K^{-1}$ and SiC can even reach 490 $W \cdot m^{-1} \cdot K^{-1}$ [13, 14]. However, their high compression modulus leads to a high thermal contact resistance [15, 16]. In contrast, some soft materials, such as rubber and resin, can fit well into the tiny voids of the mating surfaces [17]. Yet, they show poor performance because of the low thermal conductivity (0.1–0.4 $W \cdot m^{-1} \cdot K^{-1}$) [18]. Consequently, conventional TIMs combine the benefits of the aforementioned two materials, i.e., a soft material matrix (e.g., grease and polymer) with a certain mass fraction of highly

---

Address correspondence to Yiwei Sun, sunyiwei@seu.edu.cn; Menglong Hao, haom@seu.edu.cn

thermally conductive fillers, such as aluminum nitride (AlN), boron nitride (BN), nano-metal, or diamond particles. In most cases, the thermal conductivity of TIMs manufactured by this method is less than 10 W·m^{-1}·K^{-1} [7, 19, 20]. With the continuous development of high-power and high-frequency devices, however, conventional TIMs are confronted with unprecedented challenges. Other than the unsatisfactory thermal performance, such grease-based composites experience phase separation and pump-out issues during long-term use [21]. Furthermore, as an effect of operational thermal cycles, the aging of certain polymers is accelerated, resulting in a sharp increase in stiffness. Therefore, in light of the increasing heat dissipation requirements of electronic products, there is an urgent need to develop a TIM with better phase stability, higher thermal conductivity, lower compression modulus, and better cyclic durability.

In recent years, low-dimensional materials with ultra-high thermal conductivity, such as hexagonal boron nitride (hBN, ~ 500 W·m^{-1}·K^{-1}), graphene (~ 3500 W·m^{-1}·K^{-1}), and carbon nanotubes (CNTs, ~ 3000 W·m^{-1}·K^{-1}), have received increasing attention for electronic cooling applications [22–27]. In particular, vertically aligned carbon nanotube arrays (VACNTs) with their low compressive stiffness, high thermal conductivity. and good thermal and chemical stability are extensively studied as candidates for TIM and have shown promising results [28–30]. However, there are still several key issues that are prohibiting further enhancement in their properties and real-world applications. Firstly, despite the high intrinsic thermal conductivity of CNTs, the contact between the tip of VACNTs and the opposite substrate typically has a large thermal resistance [31–35]. This phenomenon results from the small fill fraction (typically 1%–5%) of the array, nonuniformity in array height and the weak bonding (van der Waals interaction) at the contact site [36–40]. All three effects contribute to atomic bonding discontinuities at the interface [41, 42]. Many studies have been aiming at improving the bonding of carbon nanotube tips to mating surfaces, including the use of organic materials and metals with a low melting point [6, 42–44]. However, these techniques require VACNTs to be directly grown on target substrates, that is, either the chip die or the heat sink surface, and some wet chemical processes that are undesirable for implementation in electronic packaging [45]. Secondly, the environment of the chemical vapor deposition (CVD) technique used to synthesize high-quality VACNTs is harsh (typically, synthesis temperatures above 650 °C) and also incompatible with device packaging processes [46]. Finally, because the individual CNTs within VACNTs grow more or less upright guided by van der Waals forces without much mutual physical contact, phonons can only propagate efficiently in the direction of the tubes [47]. This effect results in very low in-plane (perpendicular to the tubes) thermal conductivity (0.02–0.1 W·m^{-1}·K^{-1}), which is a property critical for cooling hot spots as we will show later [48–51].

Here, we propose a "transfer-and-encapsulate" strategy for preparing VACNTs-based TIM to obtain a Cu-VACNTs-Cu sandwich structure by soldering both ends of the carbon nanotubes array to copper microfoils. The standalone TIM resulting from this approach can be easily integrated into electronic packaging processes without the need for further modifications. In Cu-VACNTs-Cu, the soldered copper microfoils have a high thermal conductivity and therefore spread heat effectively from "hot spots" along the horizontal plane. In addition, due to the low thickness of the copper microfoils and this unique sandwich structure, the constructed Cu-VACNTs-Cu retains the excellent mechanical compliance of VACNTs with a nanoindentation hardness of only 24.8 MPa and a Young's modulus of 1.05 GPa. The Cu-VACNTs-Cu reaches a high through-plane thermal conductivity (parallel to the individual CNTs) of 35.6 W·m^{-1}·K^{-1}, and its thermal interface performance is examined on a real LED chip heat dissipation test rig, demonstrating substantial advantages over state-of-the-art commercial TIMs.

2 Experimental

2.1 Materials

Single-side polished Si wafers (with 280 nm thermal oxide layer) were purchased from Kaihua Crystal Core Silicon Materials Co., Ltd. The diameter and thickness of the Si wafer were 150 ± 0.3 mm and 625 ± 25 μm, respectively. Gases with purity of 99.99 % (including argon, hydrogen, and ethylene) were purchased from Nanjing Special Gas Plant Co., Ltd. The high-purity copper microfoils were provided by Anhui Zhengying Technology Co., Ltd. The thickness of the copper microfoil was 5 ± 0.2 μm and 10 ± 0.3 μm respectively. Solders ($Sn_{96.5}Ag_3Cu_{0.5}$: 25 μm thickness and 217 °C melting point, $In_{97}Ag_3$: 25 μm thickness and 158 °C melting point) were purchased from Panadar Soldering products and Electronic Chemical Products Co., Ltd. The chemicals used in the tests were reagent grade and did not require further purification.

2.2 Synthesis of VACNTs

VACNTs were fabricated on a single-crystalline Si wafer substrate (1 cm × 1 cm) using a CVD system. First, the substrates were adequately cleaned. Three catalyst layers consisting of 3 nm Ti, 6 nm Al_2O_3, and 5 nm Fe were deposited on the Si wafers by the magnetron sputtering method. The substrates were then placed in a CVD chamber and heated to 800 °C at 15 °C·min^{-1} in a mixed atmosphere of $Ar:C_2H_4:H_2$ = 120 sccm:80 sccm:50 sccm. VACNTs with a height of approximately 75 μm were obtained after growing at 800 °C for 10 min under the pristine atmosphere. Scanning electron microscopy (SEM) and transmission electron microscopy (TEM) images of typical CNTs are shown in Fig. S1 in the Electronic Supplementary Material (ESM).

2.3 Transfer of VACNTs and construction of Cu-VACNTs-Cu

Titanium, nickel, and gold were deposited on the surface of VACNTs by electron beam evaporation technique (VZS-600 Pro). The thicknesses of titanium, nickel, and gold were 50, 200, and 50 nm, respectively. The titanium enhanced the adhesion of the CNTs to the other metal layers. The nickel prevented the diffusion of the gold atoms. The gold layer was the active bonding surface for soldering to the solder. The solder ($Sn_{96.5}Ag_3Cu_{0.5}$) was placed on a copper microfoil (10 μm), and then the VACNTs (facing downward) were placed in close contact with the former. The sandwich structure of VACNTs and solder was pressed and fixed on a custom-made stainless steel fixture. The samples were soldered in a tube furnace under a vacuum better than 5 × 10^{-3} Torr and heated according to a preset temperature cycle (details can be seen in Fig. S2 in the ESM). Subsequently, the samples were naturally cooled to room temperature. Finally, the copper microfoil, solder, and VACNTs were carefully peeled off from the native growth substrate, thus completing the transfer of VACNTs from the growth substrate to the copper microfoil (Cu-VACNTs). The SEM images of the transferred VACNTs are shown in Fig. S3 in the ESM. Similarly, one side of the Cu-VACNTs and another copper microfoil were clamped tightly on the second solder ($In_{97}Ag_3$). The copper microfoil was at the bottom, and the Cu-VACNTs-Cu sandwich structure was assembled using the same soldering method as in the previous step.

2.4 Characterizations

Samples were observed for microscopic morphology using a field emission scanning electron microscope (Quanta 200, FEI, USA) and a high-resolution transmission electron microscope (Talos F200X, Thermo Fisher, USA). Three-dimensional (3D) surface profilometer (MicroXam100, KLA-Toncor, USA) was applied to characterize the top micromorphology of the copper template. The thermal diffusion coefficients of the samples were tested by the laser flash method (LFA467, Netzsch, Germany). An infrared camera was used to capture images of the temperature distribution during thermal demonstrations.

3 Results and discussion

3.1 Structural characterization of Cu-VACNTs-Cu

We accomplished the transfer and encapsulation of VACNTs using ultra-thin copper microfoil (~ 5 μm) and solder alloys in a two-step process. Figure 1(a) shows a schematic of the synthesis route of Cu-VACNTs-Cu, and more detailed information about the VACNTs can be found in Fig. S1 in the ESM. The first soldering occurs between the free ends of the VACNTs and the first copper microfoil. VACNTs' bonding to the copper microfoil is stronger than that to the growth substrate, and the transfer of VACNTs is easily accomplished by mechanical peeling. Figure S3 in the ESM shows the effectiveness of this transfer method and the micro-morphologies of the material. The second soldering was then carried out to fully encapsulate the VACNTs with copper microfoils on both ends, and the practical scale sample can be seen in Fig. S4 in the ESM. Figure 1(b) demonstrates the VACNTs in a millimeter-scale uniform and continuous composite structure achieved by our transfer-encapsulation strategy. Cross-sectional images of the entire structure are also presented in Figs. 1(c) and 1(d), showing that the soldering occurs only on the surface of the VACNTs without excessive penetration of the solder into the interior of the array, which would otherwise harm the mechanical and thermal properties of the VACNTs. Raman spectroscopy further confirms that the transfer and encapsulation steps used in our strategy do not affect the quality of the original CNTs (Fig. S5 in the ESM). It is clear from Fig. 1(e) that there are voids of micron size inside the solder layer. This is a solder defect caused by flux volatilization at high temperatures. It is worth noting that the original VACNTs do not need to have a very uniform height, because the solder melt is fluid enough to fill the gap between the copper microfoil and the rough VACNTs surface to achieve good bonding. The spatial distribution of the elements within the sandwich structure confirms the successful construction of the Cu-VACNTs-Cu (Fig. 1(f)). The bottom of the blue dashed box is the secondary electron picture of the energy dispersive spectrometer (EDS) region (rotated 90). The lower apparent intensity of Cu and In signals on the bottom side is likely due to the relative angle of the EDS detector. To further verify the effectiveness of

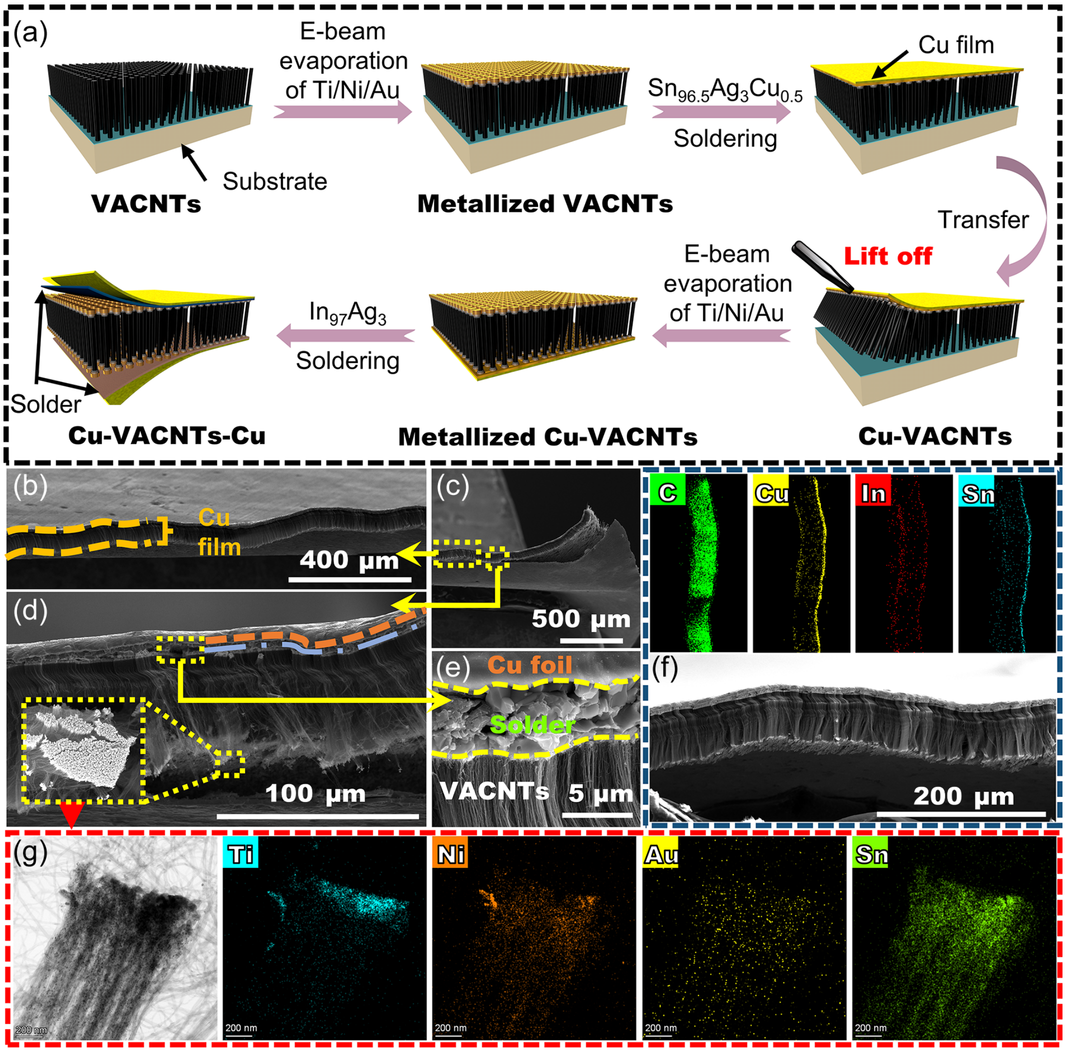

Figure 1 Fabrication process and characterization of Cu-VACNTs-Cu. (a) Schematics of the synthesis route of Cu-VACNTs-Cu. (b)–(e) Cross-sectional SEM images of the Cu-VACNTs-Cu structure. The inset in (d) is the high magnification SEM image of the CNTs at the tip after intentional disruption of the soldered interface. (f) Elemental mappings of the Cu-VACNTs-Cu (side view). (g) TEM and EDS mapping images of the CNTs end after soldering and intentional rupture.

the soldering, we intentionally ruptured the CNT-solder ($Sn_{96.5}Ag_3Cu_{0.5}$) interface and took the tips of the CNTs for observation under TEM. Figure 1(g) is the TEM image and EDS mappings of the CNTs tips. Many metal particles are attached to the tips of the CNTs. The EDS mappings show that the CNTs tips have a large amount of Sn elements in addition to the pre-evaporated Ti, Ni, and Au, suggesting that the solder has good wettability with CNTs and infiltrated the array tips by at least a micrometer.

3.2 Mechanical properties of Cu-VACNTs-Cu

One of the major benefits of using vertically aligned nanostructures for TIMs is their flexibility, which enables them to conform more easily to the mating surface roughness and reduce thermal contact resistance [7, 52, 53]. Therefore, we measured Young's modulus and hardness of polyimide film (as a benchmark), Cu-VACNTs-Cu, and VACNTs by nanoindentation experiments using a standard Berkovich indenter. We performed 20 loading/unloading cycles (to 38 mN force in each cycle) at each spot (Fig. S6 in the ESM), and nine randomly selected spots were measured for each sample. The final result was calculated by taking the mean of the nine test results. Young's modulus and hardness of the samples were calculated from the test data (force–displacement curves) using the Oliver-Pharr model [54]. More detailed information on the nanoindentation testing principles is given in Fig. S7 in the ESM. In Fig. 2(a), Young's modulus decreases with increasing loading for both polyimide and Cu-VACNTs-Cu. For polyimide, this trend (Young's modulus gradually decreases from 6.97 ± 0.24 to 2.12 ± 0.09 GPa) is commonly observed and can be well explained by the higher order displacement gradient of the polymers under the Berkovich indenter [17, 55]. For Cu-VACNTs-Cu, whose Young's modulus decreases from 1.62 ± 0.08 to 1.05 ± 0.05 GPa, we hypothesize that it is related to the inhomogeneous plastic deformation in the top Cu microfoil [56–58]. These test results show that Cu-VACNTs-Cu has a Young's modulus that is two orders of magnitude lower than that of Cu, only a third as high as that of polyimide, and comparable to that reported for pure copper-tin nanowire arrays as a TIM (~ 1 GPa) [54]. Figure 2(b) shows the results of the hardness tests for the above three materials, where the hardness is about 257 ± 145 MPa for polyimide, 68 ± 25 MPa for Cu-VACNTs-Cu, and 1.37 ± 0.25 MPa for VACNTs.

In addition, we recorded the force–displacement curves of bulk Cu, polyimide film, Cu-VACNTs-Cu, and VACNTs up to a depth of 15 μm (Fig. 2(c)). It can be seen that when the indenter displacement reaches the set value of 15 μm, the forces applied to the polyimide film, Cu-VACNTs-Cu, and VACNTs are 455, 27, and 137 mN, respectively. These low modulus and hardness of the Cu-VACNTs-Cu confirm that the mechanical compliance and deformability of VACNTs is largely preserved despite the encapsulation by Cu, a material with high intrinsic modulus, thanks to the unique micro-sandwich structure [59]. These mechanical properties are vital for the performance of Cu-VACNTs-Cu in TIM applications.

Furthermore, we also notice that the force–displacement curve of Cu-VACNTs-Cu in Fig. 2(c) shows similarity with that of VACNTs in general trend, but differs in magnitude and trend details, both of which are rooted in their respective deformation mechanisms. To investigate their microscale mechanical behavior in depth, we conducted an *in situ* indentation experiment under an SEM. A holder for SEM *in situ* measurements (ST1500, Nanofactory Instruments AB) with a 10 μm diameter indentation

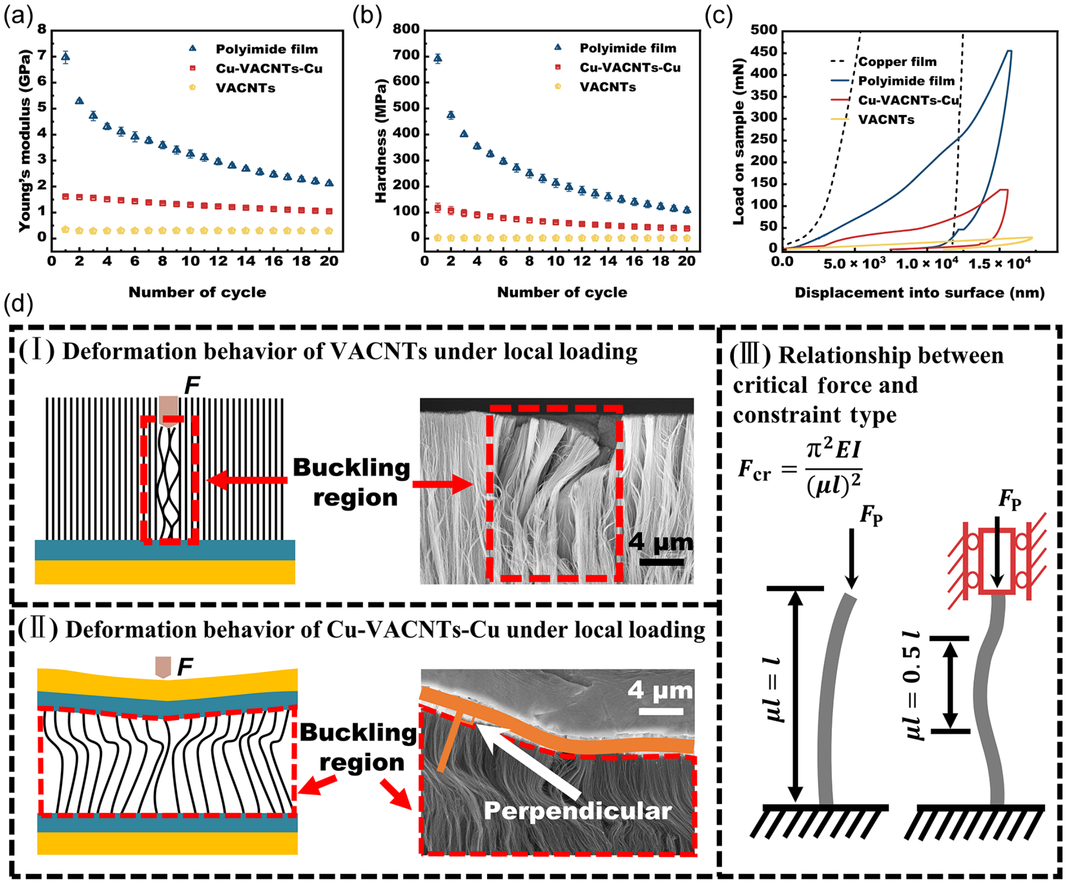

Figure 2 Characterization of mechanical properties of samples. (a) The Young' modulus of polyimide film, Cu-VACNTs-Cu, and VACNTs measured at each load cycle. (b) The hardness of polyimide films, Cu-VACNTs-Cu, and VACNTs measured at each load cycle. (c) The applied load as a function of the displacement into the surface for copper film, polyimide film, Cu-VACNTs-Cu, and VACNTs with the same largest deformation (approximately 15 μm). (d) Analysis of the structural deformation of VACNTs and Cu-VACNTs-Cu.

probe was used and the sample's deformation was observed closely (Fig. S8 in the ESM). Figures 2(d)(I) and 2(d)(II) are schematic diagrams and SEM images of VACNTs and Cu-VACNTs-Cu under compression. For VACNTs (Fig. 2(d)(I)), due to the rather weak interaction/entanglement between individual CNTs, only a small portion of the arrays right under the indenter are compressed. For Cu-VACNT-Cu (Fig. 2(d)(II)), however, the soldering connects most of the CNTs' top end into a holistic element, so a much larger number of CNTs are compressed. As Cu-VACNTs-Cu and VACNTs are compressed further, the CNTs will inevitably buckle. Based on the results of previous studies [60–63], the buckling that occurs when CNTs are compressed can be described by Euler beam theory, and by solving the differential equation of the deflection curve, we can obtain the critical load of the column (Fig. 2(d)(III)) [64], i.e.,

$$F_{\mathrm{cr}} = \frac{\pi^2 EI}{(\mu l)^2} \tag{1}$$

where l is the length of the CNT and E is Young's modulus of the CNT. I is the moment of inertia of the tube's cross-section in the direction of instability. For CNTs, $I = \pi(D^4 - d^4)/64$. D and d are the outer and inner diameters of the CNTs, respectively. μ is the length factor, which depends on the type of support the tube is subjected to.

For Cu-VACNTs-Cu, the length coefficient is taken as $\mu = 0.5$ because both sides of the VACNTs are fixedly due to the soldering. The SEM image on the right side of Fig. 2(d)(II) demonstrates that after compression, the end of the CNT remains perpendicular to the Cu microfoil, which is strong evidence of the fixed constraint. For VACNTs, its constraint type is free at the top end and fixed at the bottom end (Fig. 2(d)(I)), and the value of μ is taken as 2.0 [13]. That is, the critical forces of CNTs inside Cu-VACNTs-Cu are considerably higher than those in VACNTs at the same order of flexural modes.

3.3 Thermal properties of Cu-VACNTs-Cu

Thermal transport properties such as thermal interface resistance (TIR) and thermal conductivity are the main metrics of performance for TIMs [54, 65]. The TIR measurements of the samples in this study were conducted using the one-dimensional steady-state reference bar method based on ASTM D5470 (Fig. S9 in the ESM) on a house-made apparatus [66]. As is shown in Fig. 3(a), the TIR of the Cu-VACNTs-Cu is 70.72 ± 0.27 $\mathrm{mm^2{\cdot}K{\cdot}W^{-1}}$ at a common packaging pressure (0.5 MPa). This value is comparable to the TIR results reported by Xu et al. [52], (65 $\mathrm{mm^2{\cdot}K{\cdot}W^{-1}}$), Pal et al. [67], (100–150 $\mathrm{mm^2\ K\ W^{-1}}$), and Zhang et al. [68] (61 ± 7 $\mathrm{mm^2{\cdot}K{\cdot}W^{-1}}$), showing that Cu-VACNTs-Cu's thermal performance is not compromised despite its advantage in integration friendliness. Due to the high intrinsic thermal conductivities of Cu and CNTs (which are confirmed by laser flash measurement as will be shown later), we speculate that the majority of this TIR come from the two interfaces between the Cu-VACNTs-Cu and the reference bar surfaces. Therefore, we applied a very thin layer of silicone grease (X-23-7921-5, Shin Etsu) on both sides of Cu-VACNTs-Cu (noted as Cu-VACNTs-Cu@Grease) to further improve these two contacts. As shown in Fig. 3(a), the TIR decreases dramatically from 70.72 ± 0.27 $\mathrm{mm^2{\cdot}K{\cdot}W^{-1}}$ for dry Cu-VACNTs-Cu to 13.32 ± 0.23 $\mathrm{mm^2{\cdot}K{\cdot}W^{-1}}$ for Cu-VACNTs-Cu@Grease (at the same packaging pressure of 0.5 MPa), achieving an 81.2% drop. Different from using grease as the sole TIM, the grease is merely used to bridge submicron gaps in Cu-VACNTs-Cu@Grease, while the larger-scale nonflatness and dynamic warpage are absorbed by the Cu-VACNTs-Cu. Due to the static nature of these submicron surface roughness as well as the low thickness/volume of the grease, the pump-out issue in Cu-VACNTs-Cu@Grease is expected to be much less severe compared with that in bulk grease TIM. Notably, Cola et al. fabricated a TIM consisting of VACNTs by directly and simultaneously synthesizing on both sides of a metal foil. They reported a low thermal resistance of

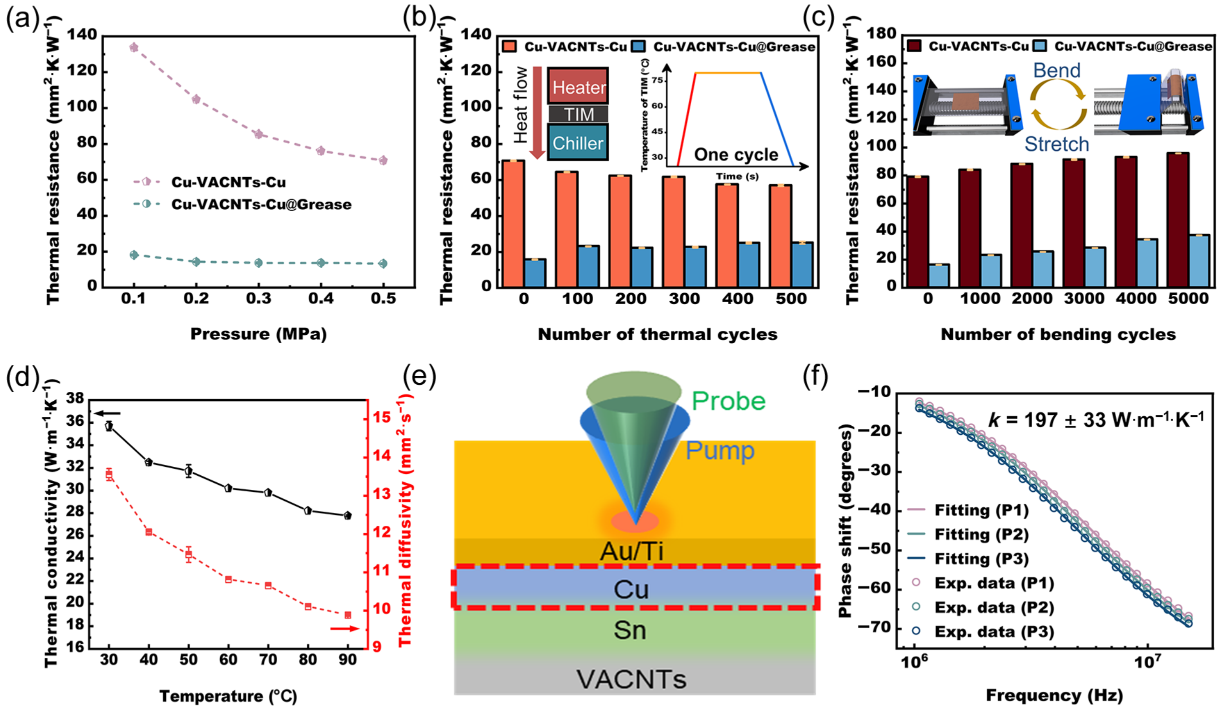

Figure 3 Characterization of thermal properties of samples. (a) The TIR of Cu-VACNTs-Cu and Cu-VACNTs-Cu@Grease as a function of applied pressure. (b) The TIR of Cu-VACNTs-Cu and Cu-VACNTs-Cu@Grease as a function of the number of thermal cycles. The illustration shows the thermal cycling device (left) and the temperature of TIM as a function of time during each cycle (right). (c) The TIR of Cu-VACNTs-Cu and Cu-VACNTs-Cu@Grease as a function of the number of bending cycles, and the illustration shows the bending device. (d) Temperature-dependent thermal conductivity of Cu-VACNTs-Cu measured by LFA. (e) A schematic of FDTR measurement on the Cu-VACNTs-Cu sample. (f) FDTR results of phase shift vs. frequency (circles) and the best fit model (solid lines) for three different points on a Cu-VACNTs-Cu sample.

10 $\mathrm{mm^2{\cdot}K{\cdot}W^{-1}}$ [69]. However, the photoacoustic method used in that study measures local thermal resistance, different from the overall area-averaged result obtained here. In addition, there was a risk of detachment of exposed CNTs potentially causing short circuit in the electronics.

The TIMs for electronic products must be able to endure alternating hot and cold environments and on-off cycles. Therefore, we conducted thermal reliability tests on the Cu-VACNTs-Cu and Cu-VACNTs-Cu@Grease by performing thermal cycles. These samples, while loaded in the test apparatus, were heated to ~ 80 °C at a rate of 200 $\mathrm{°C{\cdot}min^{-1}}$ and then naturally cooled to room temperature. The TIRs were measured every 100 thermal cycles (Fig. 3(b)). Interestingly, the TIR of the Cu-VACNTs-Cu did not increase but decreased from 70.72 ± 0.27 to 64.42 ± 0.18 $\mathrm{mm^2{\cdot}K{\cdot}W^{-1}}$ after the first 100 thermal cycles, and continued to show a slight decrease over the subsequent 400 thermal cycles and finally decreased to 56.97 ± 0.47 $\mathrm{mm^2{\cdot}K{\cdot}W^{-1}}$, which was 80.5% of the initial TIR. This behavior is very different from thermal greases, which is known to degrade over time due to pump-out and dry-out, manifested by a dramatic increase in the thermal resistance [70–72]. We attribute this phenomenon to the local plastic deformation of Cu microfoil caused by Cu microfoil softening and small relative movements during intense cyclic temperature differences [73]. As the number of thermal cycles increases, the deformation of the Cu microfoil accumulates and gradually conforms to the shape of the reference bar, creating more points of contact and thus a lower TIR. While Cu-VACNTs-Cu@Grease exhibits an opposite behavior compared to the Cu-VACNTs-Cu. Specifically, following the initial 100 thermal cycles, the TIR of the Cu-VACNTs-Cu@Grease increases from 15.75 ± 0.21 to 23.12 ± 0.15 $\mathrm{mm^2{\cdot}K{\cdot}W^{-1}}$, and then continues to slightly increase, reaching a maximum value of 25.08 ± 0.69 $\mathrm{mm^2{\cdot}K{\cdot}W^{-1}}$ after 400 thermal cycles. This behavior can be attributed to the fact that the silicone grease filled the small gaps between the Cu microfoil and the reference bar, which prevents the formation of additional points of contact despite the gradual accumulation of deformation in the Cu microfoil caused by the intense thermal cycle. Furthermore, the deteriorating performance of the silicone grease over time is manifested as an increase in TIR. In addition, we performed bending tests on Cu-VACNTs-Cu and Cu-VACNTs-Cu@Grease to examine their viability for potential use in flexible electronic applications. The experimental results indicate that both Cu-VACNTs-Cu and Cu-VACNTs-Cu@Grease TIM exhibit favorable performance even after undergoing extensive mechanical stress. Specifically, the TIR of the Cu-VACNTs-Cu increases only modestly from 79.12 ± 0.29 to 95.84 ± 0.05 $\mathrm{mm^2{\cdot}K{\cdot}W^{-1}}$ after undergoing 5000 bending cycles. Similarly, the TIR of the Cu-VACNTs-Cu@Grease also shows an upward trend, increasing from 16.35 ± 0.21 to 37.33 ± 0.19 $\mathrm{mm^2{\cdot}K{\cdot}W^{-1}}$ under the same mechanical stress conditions (Fig. 3(c)) [74]. Such a high-strain bending test would inevitably cause some minor structural damage, including some carbon nanotube tips being pulled out from the solder and delamination between the solder and the Cu microfoil. These structural damages would eventually lead to an increase in TIR.

The through-plane thermal conductivity of Cu-VACNTs-Cu was measured as a function of temperature using the LFA, and the results are present in Fig. 3(d) and Table S1 in the ESM. The thermal conductivity reaches 35.71 $\mathrm{W{\cdot}m^{-1}{\cdot}K^{-1}}$ at 30 °C as temperature increases, and the thermal conductivity gradually decreases to 27.76 $\mathrm{W{\cdot}m^{-1}{\cdot}K^{-1}}$ at 90 °C, likely due to the fact that the thermal conductivities of both Cu and CNT decrease with temperature. The through-plane thermal conductivity of Cu-VACNTs-Cu is higher than the values reported for many multiwall-VACNTs (0.5–18.6 $\mathrm{W{\cdot}m^{-1}{\cdot}K^{-1}}$) [75–82]. Furthermore, we measured the thermal conductivity of the soldered copper microfoils on the Cu-VACNTs-Cu samples using frequency domain thermoreflectance (FDTR) [83, 84]. Different from LFA, which measures the effective thermal properties of the whole sample, the FDTR method only measures the local thermal conductivity. A schematic of the FDTR experimental setup is shown in Fig. 3(e), and the red dotted box indicates the measured part of Cu-VACNTs-Cu. Figure 3(f) shows representative FDTR data measured from three different points on the Cu microfoil of the Cu-VACNTs-Cu sample. The phase shift versus frequency data were fitted to an analytical Fourier heat conduction model to determine the thermal conductivity. The measured thermal conductivities of the three points are 232, 207, and 152 $\mathrm{W{\cdot}m^{-1}{\cdot}K^{-1}}$, respectively. These values are lower than the reported value for copper microfoils (k = 290 $\mathrm{W{\cdot}m^{-1}{\cdot}K^{-1}}$, thickness = 9 μm [85]) likely because the top layer of Cu-VACNTs-Cu is actually a combination of Cu and the solder alloy, and that soldering would cause porosity. The nonuniformly distributed k (with an averaged value of 197 ± 33 $\mathrm{W{\cdot}m^{-1}{\cdot}K^{-1}}$) is attributed to copper and tin alloys' spatial inhomogeneity.

To further demonstrate the significance of laminating ultra-thin copper microfoils on both sides of VACNTs for efficient in-plane heat transfer and hot spot cooling, a finite element simulation was performed for VACNTs and Cu-VACNTs-Cu, respectively. Figure 4(a) illustrates the physical model simulating the heat dissipation near a typical hundred-micron sized electronic hot spot (more details can be seen in Table S2 in the ESM). In the model, a heat source with constant input power is applied from the top. The red dots in the schematic represent temperature probes dispersed along the TIM, corresponding to temperature value shown in Fig. 4(d). The VACNTs is modeled here as a continuous material with an effective k of 8 $\mathrm{W{\cdot}m^{-1}{\cdot}K^{-1}}$ along the through-plane direction and 0.1 $\mathrm{W{\cdot}m^{-1}{\cdot}K^{-1}}$ along the in-plane direction based on previously reported values [49, 86]. Contact thermal resistance is neglected. In these simulations, the mere difference between the VACNTs case and the Cu-VACNTs-Cu case is that VACNTs lack the copper foil soldered on both sides. The resulting highest temperature of the hot spot as a function of input power is depicted in Fig. 4(b). It can be seen that the chip die is cooler when Cu-VACNTs-Cu is used as TIM compared with that when VACNTs is used, regardless of the input power. Moreover, the difference between the highest temperature rises as the input power is continuously increased. For power electronics application, heat generation is often pulsed and the transient thermal behavior of the TIM is important. Figure 4(c) shows the transient response of the system's internal temperature distribution in the initial 1 ms of a heating pulse. In the first 0.1 ms, the heat goes only downwards from the upper surface of the die. With time, a strip-like temperature distribution is generated within the VACNTs, indicating that the heat capacity and cross-sectional area of the TIM and bottom heat sinks are not fully utilized. The temperature is the highest near the heat source and sharply decreases farther away from the heat source. The temperature profile is distinctively different for Cu-VACNTs-Cu, which has a substantially more uniform temperature distribution than VACNTs. We also extracted the probe temperature set in Fig. 4(a), and the results are shown in Fig. 4(d). It can be observed that the temperature distribution on the surface of VACNTs is strongly nonuniform. The temperature right under the hot spot is as high as 86.2 °C, while the temperature at both ends of the TIM is only 72.5 °C, resulting in a temperature difference of 13.7 °C. However, the surface temperature distribution of Cu-VACNTs-Cu is nearly unaffected by location, as the temperature is 72.0 °C near the heat source and 71.9 °C at the farthest distance from the heat source, with a variation of only 0.1 °C. The large temperature

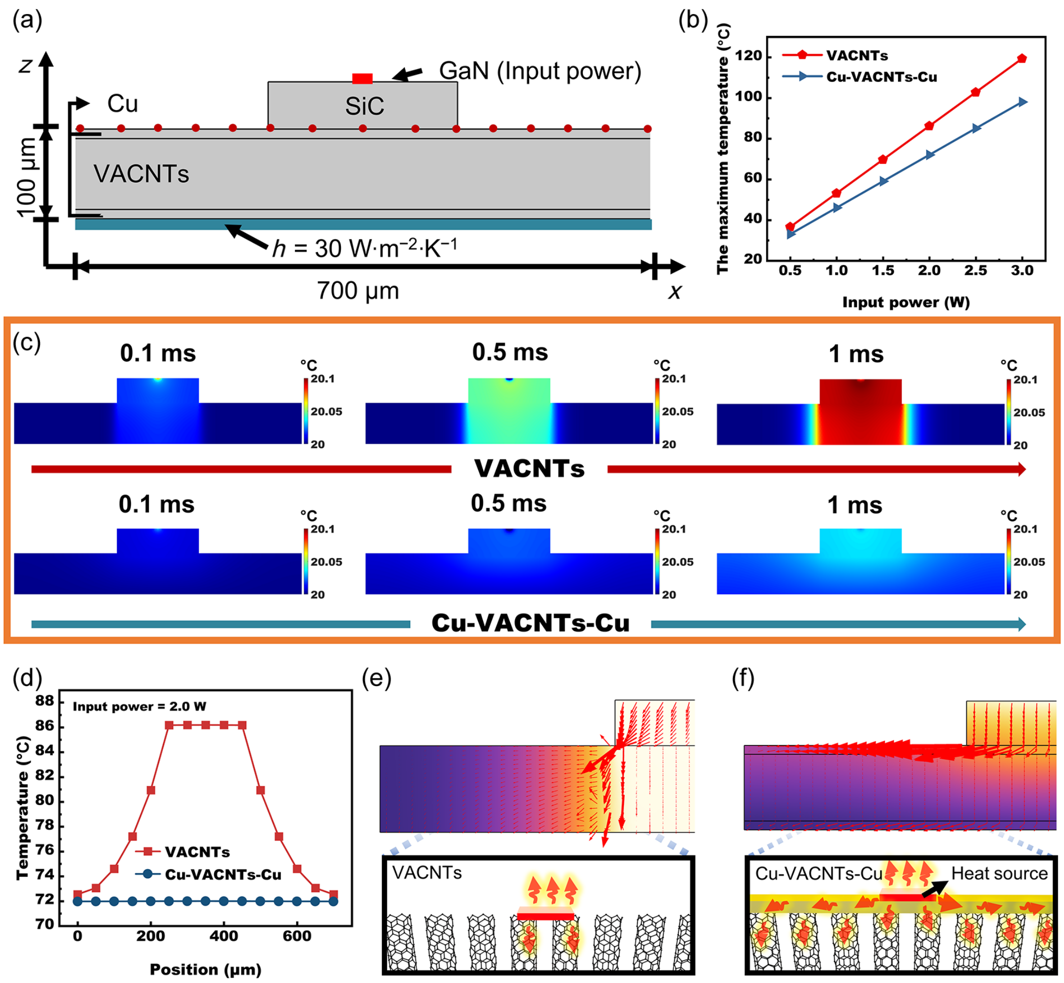

Figure 4 Finite element simulation of heat dissipation in VACNTs and Cu-VACNTs-Cu at hotspots. (a) Physical models of heat dissipation of Cu-VACNTs-Cu, and the red dots represent temperature probes in accordance with (d). (b) The simulated maximum temperature of the heat source as a function of the input power. (c) Temperature profile evolution after the onset of heat generation with an input power of 2 W. (d) The steady-state temperature measured based on the temperature probes in (a). (e) and (f) The distribution of heat flux vectors for the VACNTs and Cu-VACNTs-Cu scenarios, respectively (the size of the arrows is proportional to the magnitude of the local heat flux).

gradient in the VACNTs is the result of the high axial heat conductivity and low in-plane thermal conductivity. Only a tiny fraction of CNTs directly touching the heat source carry heat downwards (Fig. 4(e)). In contrast, in Cu-VACNTs-Cu the copper microfoil on the surface spreads heat laterally. As a result, much more CNTs make contribution to conducting heat to the heat sink, significantly boosting the effectiveness of heat dissipation (Fig. 4(f)). Thus, besides the clear benefits in packaging compatibility that we have discussed above, the Cu-VACNTs-Cu structure is also advantageous over VACNTs for hot spot cooling situations.

3.4 Characterization of the contact behavior of Cu-VACNTs-Cu

The heat transfer surfaces in real applications are not always smooth and flat as in the standard testing apparatus. Electronic products with high heat generation, as well as those exposed to large environmental temperature swings, often experience warpage and other types of deformation in the package due to thermal stress. Therefore, we investigated the contact behavior of Cu-VACNTs-Cu on an intentionally corrugated copper template (Fig. 5(a)) with a Cu foil of the same thickness as a comparison. The sample was sandwiched between the Si wafer and the copper template, only allowing deformation on the side immediately adjacent to the copper template. A custom fixture was utilized to apply force to the entire structure, thereby bringing the copper template to a complete contact with the sample. The copper template has a sinusoidal profile with an amplitude of 14 μm and a wavelength of 200 μm. Figure 5(b) is the schematic diagram showing the deformation of the Cu foil and Cu-VACNTs-Cu compressed by the copper template. Figures 5(c) and 5(d) show the corresponding *in situ* SEM images. Clearly, Cu foil cannot conformally contact the copper template, resulting in many voids between the contact surfaces, which seriously impairs heat transfer. In contrast, Cu-VACNTs-Cu readily conforms to the copper template, increasing the real contact area. Furthermore, the surface morphology of Cu-VACNTs-Cu before and after deformation was analyzed using a 3D surface profilometer with the results shown in Fig. 5(e). The corresponding surface height line scan in the *y*-direction is given in Fig. 5(f). Clearly, Cu-VACNTs-Cu follows the surface pattern of the template and exhibits the same wavelength after the compression. However, the average amplitude of Cu-VACNTs-Cu is about 7 μm, lower than that of the copper template (14 μm). The reason for this difference is that the elastic strain of Cu-VACNTs-Cu is recovered after compression. Subsequently, using the sinusoidal template as the contact surface, the TIR of Cu foil and Cu-VACNTs-Cu of the same thickness were measured (using the same one-dimensional steady-state reference bar apparatus as described earlier, albeit with a different contact surface). The results are shown in Fig. 5(g). At an initial pressure of 0.1 MPa, the TIR of Cu foil is as high as 361.08 ± 0.70 mm²·K·W⁻¹, nearly three times that of Cu-VACNTs-Cu (122.70 ± 1.09 mm²·K·W⁻¹). With a further

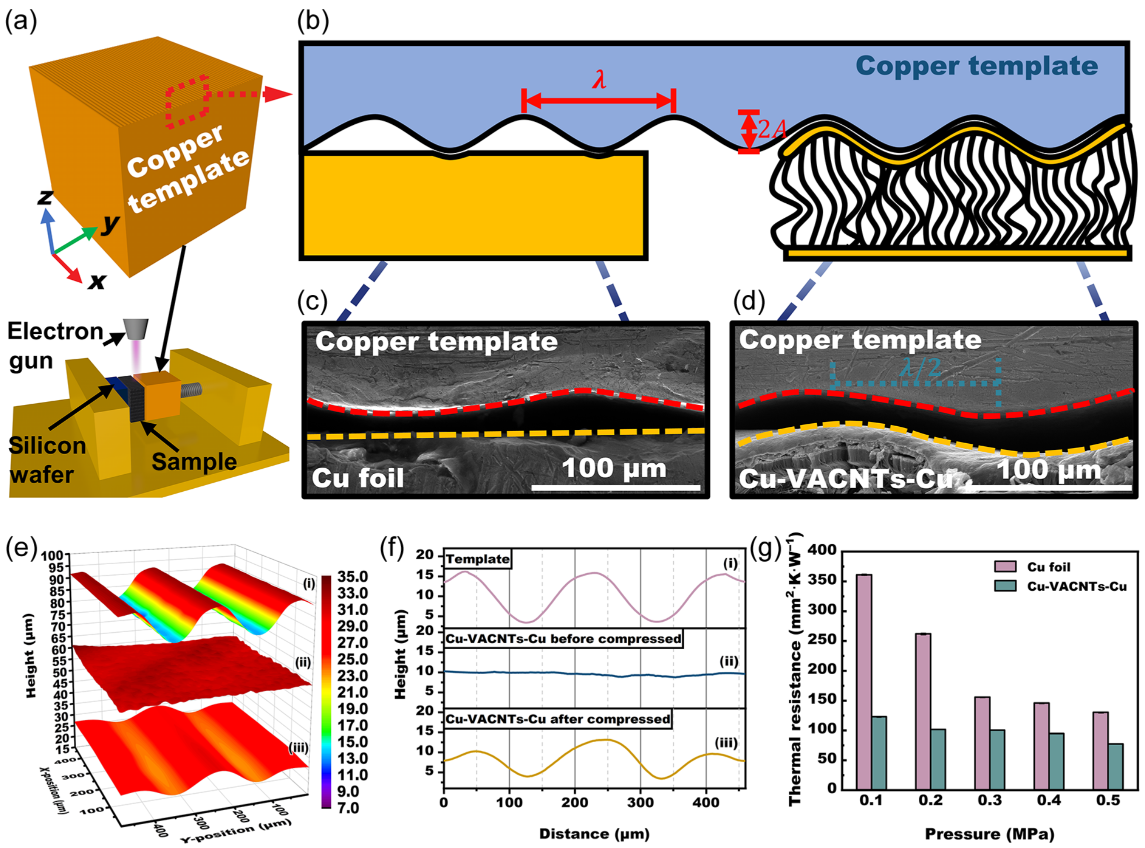

Figure 5 Characterization of the contact behavior of Cu-VACNTs-Cu on non-planar substrates. (a) Schematic diagrams of the copper template and the SEM *in situ* compression system. (b) Schematic of the mechanical contact behavior of copper foil and Cu-VACNTs-Cu under compression by the copper template, and ((c) and (d)) corresponding SEM images. ((e) and (f)) Surface micromorphology of (i) copper template, (ii) Cu-VACNTs-Cu before compression, and (iii) Cu-VACNTs-Cu after compression. (g) TIR of Cu foil and Cu-VACNTs-Cu when using the corrugated copper template as the contact surface.

increase in pressure (before 0.3 MPa), the TIR of Cu foil decreases significantly, but the decrease slows down after 0.3 MPa. In contrast, the TIR of Cu-VACNTs-Cu does not vary as drastically as that of Cu foil throughout the test and is always lower than that of the TIR of Cu foil, showing high performance for even the intentionally corrugated contact surfaces. It is noteworthy that the TIR of Cu-VACNTs-Cu exhibits a significant decrease when the pressure is increased to 0.5 MPa, despite remaining stable within the range of 0.2 to 0.3 MPa. We attribute this sudden change in TIR to a corresponding change in the structure of Cu-VACNTs-Cu, which is elaborately illustrated in Fig. S12 in the ESM.

3.5 Thermal management performance of Cu-VACNTs-Cu

To fully evaluate the cooling performance of Cu-VACNTs-Cu relative to other state-of-the-art TIMs in real applications, various TIMs were tested for LED cooling. As shown in Fig. 6(a), the LED (rated at 12 W) is electrically operated and served as the heat source. A thermocouple is affixed to the resin layer of the LED to measure its temperature. The TIMs developed in the present study are tested and compared against top-tier commercial TIMs including a thermal pad (HD90000, Laird) and a silicone grease (X-23-7921-5, Shin Etsu). It was ensured that all TIMs sandwiched between the LED chip and the heat sink have the same size (1 cm × 1 cm). The bottom heat sink is air-cooled using a powerful cooling fan. A power supply (Keithley DAQ6510) is used to send 30, 50, 70, and 90 mA currents and hold 180 s for every stage to ensure that the system reaches steady state. The temperature of the LED as a function of the time is shown in Fig. 6(b), with Indium foil as a benchmark which is one of the best TIM today. Notably, the dry Cu-VACNTs-Cu exhibits essentially the same cooling performance as the grease (with nearly inseparable temperature curves), giving better results than the thermal pad, whether the silicon grease is used or not. The results indicate that adding grease to the Thermal Pad does improve its heat transfer performance albeit only marginally. This result is expected since the TIR of Thermal Pad is dominated by its bulk thermal resistance. Regarding the Cu microfoil@Grease configuration, its performance was found to be comparable to that of the configuration using only silicon grease. This is attributed to the fact that while copper has a high thermal conductivity, the thickness of the copper foil is too thin to significantly improve the TIR of the Cu microfoil@Grease configuration. Among all the TIMs tested, Cu-VACNTs-Cu@Grease is the best performing, leading to the lowest LED temperature. At the highest current value of 90 mA, the temperature of the LED chip with Cu-VACNTs-Cu@Grease as the TIM is 10 °C lower than the chip temperature when silicone grease is used alone. Remarkably, this temperature is even lower than that when using Indium foil as the TIM, with a difference of approximately 16 °C (Fig. 6(c)). These results are further confirmed by IR thermometry images as shown in Fig. 6(d). When an electronic device is turned ON or OFF, a sudden change in heat generation will cause rapid rise or fall in temperature, which in turn may lead to severe thermomechanical stress. Therefore, we also tested these TIMs against 60 thermal shock cycles with the results present in Fig. 6(e). The experiments are performed using the same setup as in Fig. 6(a) and a LED with higher power capability (rated at 15 W). The complete thermal shock includes running the LED at 3.6 W power for 50 s ("ON" state), and then keeping the power shut ("OFF" state) for 30 s (Fig. 6(f)). Compared with the state-of-the-art grease, Cu-VACNTs-Cu@Grease consistently reduces the LED temperature by roughly 17 °C (111.25 °C vs. 94.44 °C). Due to Ye' research [87], the decrease in temperature corresponds to a 180% longer expected

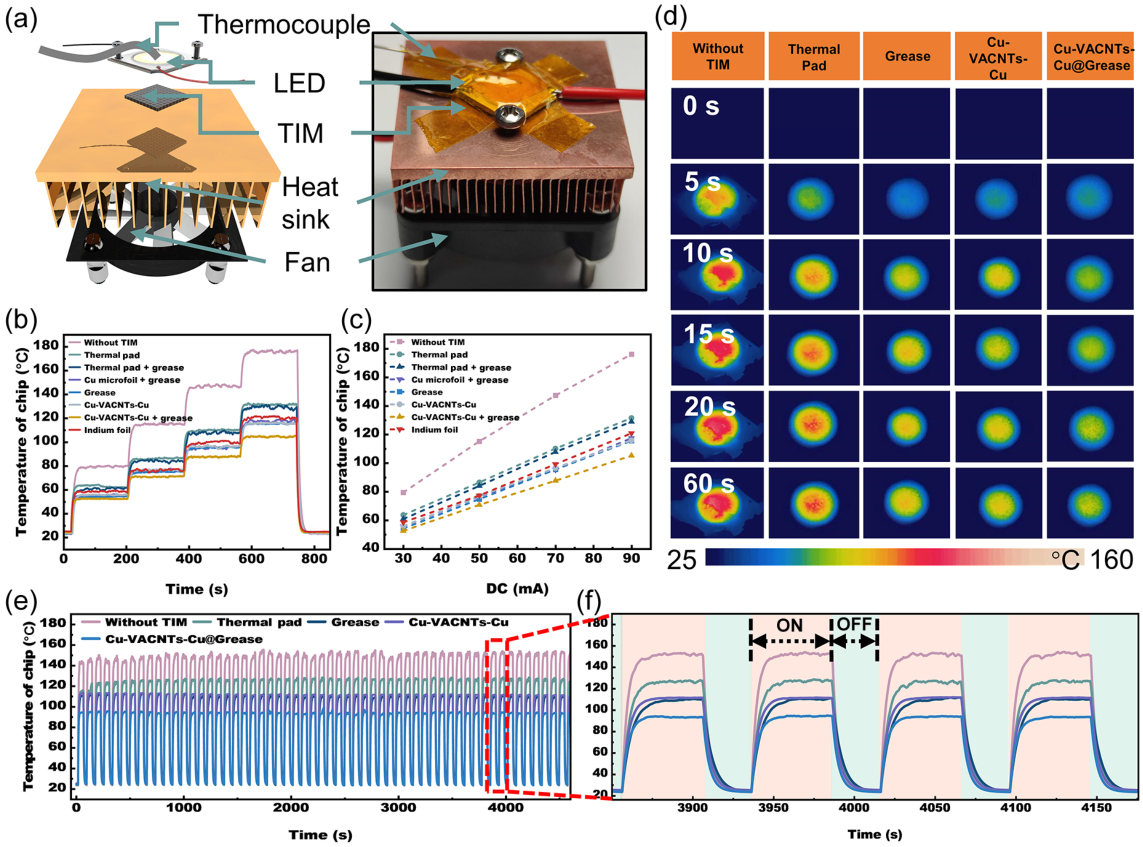

Figure 6 Demonstration of TIM's actual heat dissipation performance. (a) A schematic and a photo of the electronic package for thermal demonstration. (b) The transient temperatures of the LED as a function of time plotted in four steps: 30, 50, 70, and 90 mA, respectively, with each stage time of 180 s. (c) The plot of the steady-state temperature of the LED chip surface as a function of current. (d) IR images of the LEDs without and with different TIMs within 60 s of operation. (e) and (f) The transient temperature response of the LED chip under 60 cycles of transient thermal shock without and with different TIMs. The LED was controlled to run at 3.6 W for 50 s and then stopped for 30 s in one thermal shock cycle.

lifetime. The highest temperature of the LED loaded with Cu-VACNTs-Cu is nearly constant and actually experiences a slight decrease of roughly 1 °C over the 60 thermal shock, indicating that Cu-VACNTs-Cu and Cu-VACNTs-Cu@Grease can maintain an extremely stable heat dissipation performance under thermomechanically demanding conditions. In summary, our Cu-VACNTs-Cu and Cu-VACNTs-Cu@Grease TIMs have demonstrated equally or more effective heat dissipation properties than the state-of-the-art thermal pads or silicone greases used for electronic cooling, in addition to their intrinsic advantages in reliability (much less or no pump-out issues).

4 Conclusions

In this study, we propose a "transfer-encapsulation" strategy to prepare VACNTs-based TIM to obtain a Cu-VACNTs-Cu sandwich structure by soldering both ends of the carbon nanotubes array to copper microfoils. Cu-VACNTs-Cu retains excellent mechanical flexibility with a nanoindentation hardness of only 24.8 MPa and a Young's modulus of 1.05 GPa, as a result of rational structural design. In addition, simulations and experiments have demonstrated that in Cu-VACNTs-Cu, the soldered copper microfoil has a high thermal conductivity and can therefore spread heat efficiently from the "hot spot" along the horizontal plane. The TIM performance evaluation demonstrates substantial advantages over state-of-the-art commercial TIMs. This study not only proposes a design concept for high-performance TIMs, but also provides a solution to the longstanding problem of incompatibility between VACNTs and current packaging workflow. The findings may accelerate practical application of VACNTs in electronic thermal management.

Acknowledgements

This work was supported by the National Natural Science Foundation of China (No. 52076041), the Natural Science Foundation of Jiangsu Province (No. BK20200371), and the Nanjing Carbon Peak and Carbon Neutrality Science and Technology Innovation Project (No. 202211009). We thank the Big Data Computing Center of Southeast University for providing the facility support on the numerical calculations in this paper.

Electronic Supplementary Material: Supplementary material (further details of the mechanical characterization, TIR measurements, finite element simulation of deformation behavior of Cu-VACNTs-Cu on non-planer surfaces, thermal conductivity measurements based on LFA, and FDTR tests on the local thermal conductivity of samples; microscopic characterization of VACNTs; temperature during soldering as a function of time for $Sn_{96.5}Ag_3Cu_{0.5}$ and $In_{97}Ag_3$; characterization of the transferred VACNTs; image of practical scale sample; Raman spectra of pristine CNT, transferred CNT, and encapsulated CNT; the load/unload function applied on the sample; force versus displacement of Cu-VACNTs-Cu under cyclic loading; *in-situ* nanomechanical testing modes (ST1500, Nanofactory Instruments AB) in the SEM sample cavity; schematic of one-dimensional steady state thermal resistance measurement system, specific heat capacity of Cu-VACNTs-Cu as a function of temperature, the result of simulated temperature distribution when VACNTs and Cu-VACNTs-Cu are used as TIMs within 1 ms, finite element simulation results of deformation behavior of Cu-VACNTs-Cu on non-planer surfaces, the parameters for calculating the thermal conductivity of Cu-VACNTs-Cu as a function of temperature; the detailed parameters of the components in the simulated system) is available in the online version of this article at https://doi.org/10.1007/s12274-023-5872-y.

References

[1] Ferain, I.; Colinge, C. A.; Colinge, J. P. Multigate transistors as the future of classical metal-oxide-semiconductor field-effect transistors. *Nature* **2011**, *479*, 310–316.

[2] Moore, A. L.; Shi, L. Emerging challenges and materials for thermal management of electronics. *Mater. Today* **2014**, *17*, 163–174.

[3] Maqbool, M.; Guo, H. C.; Bashir, A.; Usman, A.; Abid, A. Y.; He, G. S.; Ren, Y. J.; Ali, Z.; Bai, S. L. Enhancing through-plane thermal conductivity of fluoropolymer composite by developing *in situ* nano-urethane linkage at graphene–graphene interface. *Nano Res.* **2020**, *13*, 2741–2748.

[4] Guo, X. X.; Cheng, S. J.; Yan, B.; Li, Y. L.; Zhou, Y. H.; Cai, W. W.; Zhang, Y. F.; Zhang, X. A. Extraordinary thermal conductivity of polyvinyl alcohol composite by aligning densified carbon fiber via magnetic field. *Nano Res.* **2023**, *16*, 2572–2578.

[5] Pop, E. Energy dissipation and transport in nanoscale devices. *Nano Res.* **2010**, *3*, 147–169.

[6] Tong, T.; Zhao, Y.; Delzeit, L.; Kashani, A.; Meyyappan, M.; Majumdar, A. Dense vertically aligned multiwalled carbon nanotube arrays as thermal interface materials. *IEEE Trans. Comp. Packag. Technol.* **2007**, *30*, 92–100.

[7] Dai, W.; Ma, T. F.; Yan, Q. W.; Gao, J. Y.; Tan, X.; Lv, L.; Hou, H.; Wei, Q. P.; Yu, J. H.; Wu, J. B. et al. Metal-level thermally conductive yet soft graphene thermal interface materials. *ACS Nano* **2019**, *13*, 11561–11571.

[8] Bar-Cohen, A.; Matin, K.; Narumanchi, S. Nanothermal interface materials: Technology review and recent results. *J. Electron. Packag.* **2015**, *137*, 040803.

[9] Prasher, R. Thermal interface materials: Historical perspective, status, and future directions. *Proc. IEEE* **2006**, *94*, 1571–1586.

[10] Schmidt, A. J.; Collins, K. C.; Minnich, A. J.; Chen, G. Thermal conductance and phonon transmissivity of metal–graphite interfaces. *J. Appl. Phys.* **2010**, *107*, 104907.

[11] Xu, S. C.; Cheng, T.; Yan, Q. W.; Shen, C.; Yu, Y.; Lin, C. T.; Ding, F.; Zhang, J. Chloroform-assisted rapid growth of vertical graphene array and its application in thermal interface materials. *Adv. Sci.* **2022**, *9*, 2200737.

[12] Xu, S. C.; Zhang, J. Vertically aligned graphene for thermal interface materials. *Small Struct.* **2020**, *1*, 2000034.

[13] Shackelford, J. F.; Alexander, W. *CRC Materials Science and Engineering Handbook*; 3rd ed. CRC Press: Boca Raton, 2000.

[14] Nath, P.; Chopra, K. L. Thermal conductivity of copper films. *Thin Solid Films* **1974**, *20*, 53–62.

[15] Chung, D. D. L. Performance of thermal interface materials. *Small* **2022**, *18*, 2200693.

[16] Chen, W.; Zhang, J. C.; Yue, Y. N. Molecular dynamics study on thermal transport at carbon nanotube interface junctions: Effects of mechanical force and chemical functionalization. *Int. J. Heat Mass Transf.* **2016**, *103*, 1058–1064.

[17] Alisafaei, F.; Han, C. S. Indentation depth dependent mechanical behavior in polymers. *Adv. Condens. Matter Phys.* **2015**, *2015*, 391579.

[18] Zhang, Y. L.; Ma, Z. L.; Ruan, K. P.; Gu, J. W. Multifunctional $Ti_3C_2T_x$-(Fe_3O_4/polyimide) composite films with Janus structure for outstanding electromagnetic interference shielding and superior visual thermal management. *Nano Res.* **2022**, *15*, 5601–5609.

[19] Ding, D. L.; Zhang, S. Y.; Liang, H. Y.; Wang, X.; Wu, Y.; Ye, Y. M.; Liu, Z. G.; Zhang, Q. Y.; Qin, G. Z.; Chen, Y. H. Enhancing thermal conductivity of silicone rubber composites by *in-situ* constructing SiC networks: A finite-element study based on first principles calculation. *Nano Res.* **2023**, *16*, 1430–1440.

[20] Yan, Y. Z.; Li, S. W.; Park, S. S.; Zhang, W. J.; Lee, J. S.; Kim, J. R.; Seong, D. G.; Ha, C. S. "One stone, two birds" solvent system to fabricate microcrystalline cellulose-$Ti_3C_2T_x$ nanocomposite film as a flexible dielectric and thermally conductive material. *Nano Res.* **2023**, *16*, 3240–3253.

[21] Loeblein, M.; Tsang, S. H.; Pawlik, M.; Phua, E. J. R.; Yong, H.; Zhang, X. W.; Gan, C. L.; Teo, E. H. T. High-density 3D-boron nitride and 3D-graphene for high-performance nano-thermal interface material. *ACS Nano* **2017**, *11*, 2033–2044.

[22] Zhang, Q. Q.; Lin, D.; Deng, B. W.; Xu, X.; Nian, Q.; Jin, S. Y.; Leedy, K. D.; Li, H.; Cheng, G. J. Flyweight, superelastic, electrically conductive, and flame-retardant 3D multi-nanolayer graphene/ceramic metamaterial. *Adv. Mater.* **2017**, *29*, 1605506.

[23] Jeong, G. H.; Sasikala, S. P.; Yun, T.; Lee, G. Y.; Lee, W. J.; Kim, S. O. Nanoscale assembly of 2D materials for energy and environmental applications. *Adv. Mater.* **2020**, *32*, 1907006.

[24] Kim, P.; Shi, L.; Majumdar, A.; McEuen, P. L. Thermal transport measurements of individual multiwalled nanotubes. *Phys. Rev. Lett.* **2001**, *87*, 215502.

[25] He, H.; Peng, W.; Liu, J.; Chan, X.Y.; Liu, S.; Lu, L.; Le Ferrand, H. Microstructured BN composites with internally designed high thermal conductivity paths for 3D electronic packaging. *Advanced Materials* **2022**, *34*, 2205120.

[26] Balandin, A. A. Thermal properties of graphene and nanostructured carbon materials. *Nat. Mater.* **2011**, *10*, 569–581.

[27] He, P.; Du, T.; Zhao, K. R.; Dong, J. Q.; Liang, Y. S.; Zhang, Q. Q. Lightweight 3D graphene metamaterials with tunable negative thermal expansion. *Adv. Mater.* **2023**, *35*, 2208562.

[28] Maschmann, M. R.; Zhang, Q. H.; Du, F.; Dai, L. M.; Baur, J. Length dependent foam-like mechanical response of axially indented vertically oriented carbon nanotube arrays. *Carbon* **2011**, *49*, 386–397.

[29] Ge, X.; Tay, G.; Hou, Y.; Zhao, Y.; Sugumaran, P.J.; Thai, B.Q.; Ang, C.K.; Zhai, W.; Yang, Y. Flexible and leakage-proof phase change composite for microwave attenuation and thermal management. *Carbon* **2023**, *210*, 118084.

[30] Yu, W.; Duan, Z.; Zhang, G.; Liu, C. H.; Fan, S. S. Effect of an auxiliary plate on passive heat dissipation of carbon nanotube-based materials. *Nano Lett.* **2018**, *18*, 1770–1776.

[31] Panzer, M. A.; Duong, H. M.; Okawa, J.; Shiomi, J.; Wardle, B. L.; Maruyama, S.; Goodson, K. E. Temperature-dependent phonon conduction and nanotube engagement in metalized single wall carbon nanotube films. *Nano Lett.* **2010**, *10*, 2395–2400.

[32] Aliev, A. E.; Lima, M. H.; Silverman, E. M.; Baughman, R. H. Thermal conductivity of multi-walled carbon nanotube sheets: Radiation losses and quenching of phonon modes. *Nanotechnology* **2010**, *21*, 035709.

[33] Wang, X. W.; Zhong, Z. R.; Xu, J. Noncontact thermal characterization of multiwall carbon nanotubes. *J. Appl. Phys.* **2005**, *97*, 064302.

[34] Pettes, M. T.; Shi, L. Thermal and structural characterizations of individual single-, double-, and multi-walled carbon nanotubes. *Adv. Funct. Mater.* **2009**, *19*, 3918–3925.

[35] Li, Q. W.; Liu, C. H.; Fan, S. S. Thermal boundary resistances of carbon nanotubes in contact with metals and polymers. *Nano Lett.* **2009**, *9*, 3805–3809.

[36] Marconnet, A. M.; Yamamoto, N.; Panzer, M. A.; Wardle, B. L.; Goodson, K. E. Thermal conduction in aligned carbon nanotube-polymer nanocomposites with high packing density. *ACS Nano* **2011**, *5*, 4818–4825.

[37] Panzer, M. A.; Zhang, G.; Mann, D.; Hu, X.; Pop, E.; Dai, H.; Goodson, K. E. Thermal properties of metal-coated vertically aligned single-wall nanotube arrays. *J. Heat Transf.* **2008**, *130*, 052401.

[38] Lin, W.; Moon, K. S.; Wong, C. P. A combined process of *in situ* functionalization and microwave treatment to achieve ultrasmall thermal expansion of aligned carbon nanotube-polymer nanocomposites: Toward applications as thermal interface materials. *Adv. Mater.* **2009**, *21*, 2421–2424.

[39] Huang, H.; Liu, C. H.; Wu, Y.; Fan, S. Aligned carbon nanotube composite films for thermal management. *Adv. Mater.* **2005**, *17*, 1652–1656.

[40] Zhang, G.; Liu, C. H.; Fan, S. S. Temperature dependence of thermal boundary resistances between multiwalled carbon nanotubes and some typical counterpart materials. *ACS Nano* **2012**, *6*, 3057–3062.

[41] Hao, M. L.; Kumar, A.; Hodson, S. L.; Zemlyanov, D.; He, P. G.;

Fisher, T. S. Brazed carbon nanotube arrays: Decoupling thermal conductance and mechanical rigidity. *Adv. Mater. Interfaces* **2017**, *4*, 1601042.

[42] Kaur, S.; Raravikar, N.; Helms, B. A.; Prasher, R.; Ogletree, D. F. Enhanced thermal transport at covalently functionalized carbon nanotube array interfaces. *Nat. Commun.* **2014**, *5*, 3082.

[43] Taphouse, J. H.; Smith, O. L.; Marder, S. R.; Cola, B. A. A pyrenylpropyl phosphonic acid surface modifier for mitigating the thermal resistance of carbon nanotube contacts. *Adv. Funct. Mater.* **2014**, *24*, 465–471.

[44] Barako, M. T.; Gao, Y.; Marconnet, A. M.; Asheghi, M.; Goodson, K. E. Solder-bonded carbon nanotube thermal interface materials. In *Proceedings of the 13th InterSociety Conference on Thermal and Thermomechanical Phenomena in Electronic Systems*, San Diego, CA, USA, 2012, pp 1225–1233.

[45] Yu, W.; Liu, C. H.; Fan, S. S. Advances of CNT-based systems in thermal management. *Nano Res.* **2021**, *14*, 2471–2490.

[46] Wang, M.; Li, T. T.; Yao, Y. G.; Lu, H. F.; Li, Q.; Chen, M. H.; Li, Q. W. Wafer-scale transfer of vertically aligned carbon nanotube arrays. *J. Am. Chem. Soc.* **2014**, *136*, 18156–18162.

[47] Wang, H.; Tazebay, A. S.; Yang, G.; Lin, H. T.; Choi, W.; Yu, C. Highly deformable thermal interface materials enabled by covalently-bonded carbon nanotubes. *Carbon* **2016**, *106*, 152–157.

[48] Kong, Q. Y.; Bodelot, L.; Lebental, B.; Lim, Y. D.; Shiau, L. L.; Gusarov, B.; Tan, C. W.; Liang, K.; Lu, C. X.; Tan, C. S. et al. Novel three-dimensional carbon nanotube networks as high performance thermal interface materials. *Carbon* **2018**, *132*, 359–369.

[49] Cai, Y.; Yu, H. T.; Chen, C.; Feng, Y. Y.; Qin, M. M.; Feng, W. Improved thermal conductivities of vertically aligned carbon nanotube arrays using three-dimensional carbon nanotube networks. *Carbon* **2022**, *196*, 902–912.

[50] Peng, L. Q.; Yu, H. T.; Chen, C.; He, Q. X.; Zhang, H.; Zhao, F. L.; Qin, M. M.; Feng, Y. Y.; Feng, W. Tailoring dense, orientation-tunable, and interleavedly structured carbon-based heat dissipation plates. *Adv. Sci.* **2023**, *10*, 2205962.

[51] Yu, H. T.; Feng, Y. Y.; Chen, C.; Zhang, Z. X.; Cai, Y.; Qin, M. M.; Feng, W. Thermally conductive, self-healing, and elastic polyimide@vertically aligned carbon nanotubes composite as smart thermal interface material. *Carbon* **2021**, *179*, 348–357.

[52] Xu, J.; Fisher, T. S. Enhanced thermal contact conductance using carbon nanotube array interfaces. *IEEE Trans. Comp. Packag. Technol.* **2006**, *29*, 261–267.

[53] Jing, L.; Cheng, R.; Garg, R.; Gong, W.; Lee, I.; Schmit, A.; Cohen-Karni, T.; Zhang, X.; Shen, S. 3D graphene-nanowire "sandwich" thermal interface with ultralow resistance and stiffness. *ACS Nano* **2023**, *17*, 2602–2610.

[54] Gong, W.; Li, P. F.; Zhang, Y. H.; Feng, X. H.; Major, J.; DeVoto, D.; Paret, P.; King, C.; Narumanchi, S.; Shen, S. Ultracompliant heterogeneous copper-tin nanowire arrays making a supersolder. *Nano Lett.* **2018**, *18*, 3586–3592.

[55] Alisafaei, F.; Han, C. S.; Lakhera, N. Characterization of indentation size effects in epoxy. *Polym. Test.* **2014**, *40*, 70–78.

[56] Wang, H. D.; Zhu, L. N.; Xu, B. S. *Residual Stresses and Nanoindentation Testing of Films and Coatings*; Springer: Singapore, 2018.

[57] Leitner, A.; Maier-Kiener, V.; Kiener, D. Dynamic nanoindentation testing: Is there an influence on a material's hardness. *Mater. Res. Lett.* **2017**, *5*, 486–493.

[58] Elmustafa, A. A.; Stone, D. S. Nanoindentation and the indentation size effect: Kinetics of deformation and strain gradient plasticity. *J. Mech. Phys. Solids* **2003**, *51*, 357–381.

[59] Lin, Z. S.; Dong, J. Q.; Wang, X.; Huang, Q. T.; Shen, X.; Yang, M. L.; Sun, X. X.; Yuan, Y.; Wang, S. S.; Ning, Y. H. et al. Twin-structured graphene metamaterials with anomalous mechanical properties. *Adv. Mater.* **2022**, *34*, 2200444.

[60] Tong, T.; Zhao, Y.; Delzeit, L.; Kashani, A.; Meyyappan, M.; Majumdar, A. Height independent compressive modulus of vertically aligned carbon nanotube arrays. *Nano Lett.* **2008**, *8*, 511–515.

[61] Maschmann, M. R.; Zhang, Q. H.; Wheeler, R.; Du, F.; Dai, L. M.; Baur, J. In situ SEM observation of column-like and foam-like CNT array nanoindentation. *ACS Appl. Mater. Interfaces* **2011**, *3*, 648–653.

[62] Pour Shahid Saeed Abadi, P.; Hutchens, S. B.; Greer, J. R.; Cola, B. A.; Graham, S. Buckling-driven delamination of carbon nanotube forests. *Appl. Phys. Lett.* **2013**, *102*, 223103.

[63] Li, Y. P.; Kim, H. I.; Wei, B. Q.; Kang, J. M.; Choi, J. B.; Nam, J. D.; Suhr, J. Understanding the nanoscale local buckling behavior of vertically aligned MWCNT arrays with van der Waals interactions. *Nanoscale* **2015**, *7*, 14299–14304.

[64] Bauchau, O. A.; Craig, J. I. Euler-Bernoulli beam theory. In *Structural Analysis*: *With Applications to Aerospace Structures*. Bauchau, O. A.; Craig, J. I., Eds.; Springer: Dordrecht, 2009; pp 173–221.

[65] Xu, S. C.; Wang, S. S.; Chen, Z.; Sun, Y. Y.; Gao, Z. F.; Zhang, H.; Zhang, J. Electric-field-assisted growth of vertical graphene arrays and the application in thermal interface materials. *Adv. Funct. Mater.* **2020**, *30*, 2003302.

[66] Hao, M. L.; Saviers, K. R.; Fisher, T. S. Design and validation of a high-temperature thermal interface resistance measurement system. *J. Therm. Sci. Eng. Appl.* **2016**, *8*, 031008.

[67] Zhang, X. Carbon nanotube/polyetheretherketone nanocomposites: Mechanical, thermal, and electrical properties. *Journal of Composite Materials* **2021**, *5*, 2115–2132.

[68] Zhang, K.; Chai, Y.; Yuen, M. M. F.; Xiao, D. G. W.; Chan, P. C. H. Carbon nanotube thermal interface material for high-brightness light-emitting-diode cooling. *Nanotechnology* **2008**, *19*, 215706.

[69] Cola, B. A.; Xu, X. F.; Fisher, T. S. Increased real contact in thermal interfaces: A carbon nanotube/foil material. *Appl. Phys. Lett.* **2007**, *90*, 093513.

[70] DeVoto, D.; Major, J.; Paret, P.; Blackman, G. S.; Wong, A.; Meth, J. S. Degradation characterization of thermal interface greases. In *Proceedings of the 2017 16th IEEE Intersociety Conference on Thermal and Thermomechanical Phenomena in Electronic Systems* (*ITherm*), Orlando, FL, USA, 2017, pp 394–399.

[71] Khuu, V.; Osterman, M.; Bar-Cohen, A.; Pecht, M. Effects of temperature cycling and elevated temperature/humidity on the thermal performance of thermal interface materials. *IEEE Trans. Device Mater. Reliab.* **2009**, *9*, 379–391.

[72] Razeeb, K. M.; Dalton, E.; Cross, G. L. W.; Robinson, A. J. Present and future thermal interface materials for electronic devices. *Int. Mater. Rev.* **2018**, *63*, 1–21.

[73] Hao, M. L.; Huang, Z. X.; Saviers, K. R.; Xiong, G. P.; Hodson, S. L.; Fisher, T. S. Characterization of vertically oriented carbon nanotube arrays as high-temperature thermal interface materials. *Int. J. Heat Mass Transf.* **2017**, *106*, 1287–1293.

[74] Barako, M. T.; Isaacson, S. G.; Lian, F. F.; Pop, E.; Dauskardt, R. H.; Goodson, K. E; Tice, J. Dense vertically aligned copper nanowire composites as high performance thermal interface materials. *ACS Appl. Mater. Interfaces* **2017**, *9*, 42067–42074.

[75] Ivanov, I.; Puretzky, A.; Eres, G.; Wang, H.; Pan, Z. W.; Cui, H. T.; Jin, R. Y.; Howe, J.; Geohegan, D. B. Fast and highly anisotropic thermal transport through vertically aligned carbon nanotube arrays. *Appl. Phys. Lett.* **2006**, *89*, 223110.

[76] Jakubinek, M. B.; White, M. A.; Li, G.; Jayasinghe, C.; Cho, W.; Schulz, M. J.; Shanov, V. Thermal and electrical conductivity of tall, vertically aligned carbon nanotube arrays. *Carbon* **2010**, *48*, 3947–3952.

[77] Marconnet, A. M.; Panzer, M. A.; Goodson, K. E. Thermal conduction phenomena in carbon nanotubes and related nanostructured materials. *Rev. Mod. Phys.* **2013**, *85*, 1295–1326.

[78] Okamoto, A.; Gunjishima, I.; Inoue, T.; Akoshima, M.; Miyagawa, H.; Nakano, T.; Baba, T.; Tanemura, M.; Oomi, G. Thermal and electrical conduction properties of vertically aligned carbon nanotubes produced by water-assisted chemical vapor deposition. *Carbon* **2011**, *49*, 294–298.

[79] Pal, S. K.; Son, Y.; Borca-Tasciuc, T.; Borca-Tasciuc, D. A.; Kar, S.; Vajtai, R.; Ajayan, P. M. Thermal and electrical transport along MWCNT arrays grown on inconel substrates. *J. Mater. Res.* **2008**, *23*, 2099–2105.

[80] Son, Y.; Pal, S. K.; Borca-Tasciuc, T.; Ajayan, P. M.; Siegel, R. W. Thermal resistance of the native interface between vertically aligned multiwalled carbon nanotube arrays and their SiO_2/Si substrate. *J. Appl. Phys.* **2008**, *103*, 024911.

[81] Yang, D. J.; Wang, S. G.; Zhang, Q.; Sellin, P. J.; Chen, G. Thermal and electrical transport in multi-walled carbon nanotubes. *Phys. Lett. A* **2004**, *329*, 207–213.

[82] Yang, D. J.; Zhang, Q.; Chen, G.; Yoon, S. F.; Ahn, J.; Wang, S. G.; Zhou, Q.; Wang, Q.; Li, J. Q. Thermal conductivity of multiwalled carbon nanotubes. *Phys. Rev. B* **2002**, *66*, 165440.

[83] Yang, J.; Maragliano, C.; Schmidt, A. J. Thermal property microscopy with frequency domain thermoreflectance. *Rev. Sci. Instrum.* **2013**, *84*, 104904.

[84] Ziade, E. Wide bandwidth frequency-domain thermoreflectance: Volumetric heat capacity, anisotropic thermal conductivity, and thickness measurements. *Rev. Sci. Instrum.* **2020**, *91*, 124901.

[85] Goli, P.; Ning, H.; Li, X. S.; Lu, C. Y.; Novoselov, K. S.; Balandin, A. A. Thermal properties of graphene-copper-graphene heterogeneous films. *Nano Lett.* **2014**, *14*, 1497–1503.

[86] Shaikh, S.; Li, L.; Lafdi, K.; Huie, J. Thermal conductivity of an aligned carbon nanotube array. *Carbon* **2007**, *45*, 2608–2613.

[87] Ye, C.; Chen, Y.; Kang, R. Calculation of failure rate of semiconductor devices based on mechanism consistency. In *Engineering Asset Management—Systems*, *Professional Practices and Certification*. Tse, P. W.; Mathew, J.; Wong, K.; Lam, R.; Ko, C. N. , Eds.; Springer: Cham, 2015; pp 1789–1796.